Supplementary Information for

Observations suggest that North African dust absorbs less solar radiation than models estimate.

Adeyemi A. Adebiyi[1,*], Yue Huang[2,3,4], Bjørn H. Samset[5] and Jasper F. Kok[2]

*Corresponding author: Adeyemi Adebiyi; Email: aaadebiyi@ucmerced.edu.

Table S- 1: Single-Scattering albedo (SSA) measurements compiled from the literature, including information about the representative locations, heights, dates, diameter ranges, and wavelengths. It also contains information about the method used to obtain the SSA and the diameter types (last column).

Study	Campaign name	Campaign platform	Representative location (longitude and latitude)	Representative altitude (m)	Date (Representative Season)	Diameter range (µm)	Wavelength (nm)	SSA	Uncertainty	Method to obtain SSA* and other comments.
Haywood et al.[1]	SHADE	Aircraft	Sal Islands to M'Bour Senegal 18.17°N, 19.92°W	2400 – 7200	21, 24, 25, and 28 September 2000 (SON)	0.1 – 3º	550	0.97	0.0050	Directly measured – M1; See their table 1; Table 6 of McConnell et al. (2008)
Osborne et al.[2]	DABEX	Aircraft	Northeast of Niamey, Niger 15.51°N, 4.94°E	0 – 900	21, 23, and 30 January 2006 (DJF)	0.1 – 3º	550	0.99	0.0050	Directly measured – M1; see their Table 4
McConnell et al.[3]	DODO-1	Aircraft	Dakar Senegal 17.02°N, 16.71°W	70	14 to 16 February 2006 (DJF)	0.1 – 3	550	0.9892	0.0030	Directly measured – M1; See their figure 8 and Table 6; Figure 1 of McConnell et al. (2010) for height information
				210 – 320		0.1 – 3	550	0.9952	0.0033	
				500 – 520		0.1 – 3	550	0.9932	0.0036	
				1510		0.1 – 3	550	0.9959	0.0033	
	DODO-2	Aircraft	Dakar Senegal 19.89°N, 12.5°W	52	22 to 28 August 2006 (JJA)	0.1 – 3	550	0.9980	0.0005	
				315		0.1 – 3	550	0.9780	0.0018	
				510		0.1 – 3	550	0.9954	0.0113	
				2000 – 3000		0.1 – 3	550	0.9818	0.0055	
				3000 – 4000		0.1 – 3	550	0.9747	0.0247	
				5000		0.1 – 3	550	0.9805	0.0132	
Schladitz et al.[4]	SAMUM-1	Ground-based station	Tinfou Morocco 30.24°N, 5.61°W	730 (elevation)	27 to 28 May 2006 (MAM)	0.07 – 6.7	537	0.9573	0.0021	Directly measured – M2; aerodynamic diameter; See their
							637	0.9777	0.0025	

										figure 9a – high dust
Chen et al.[5]	NAMMA	Aircraft	Cape Verde Islands 16.81°N, 22.37°W	1520 – 3690	15 August to 20 September 2006 (SON)	0.5 – 3.4	470	0.95	0.010	Directly measured – M1.5; aerodynamic diameter; see their Table 5
							532	0.97	0.010	
							670	0.99	0.010	
Formenti et al.[6]	AMMA	Aircraft	Banizoumbou Niger 13.52°N, 2.63°E	300 – 5300	11 June 2006 (JJA)	0.1 – 9	370	0.9102		Directly measured – M3; See their figure 11 and Table 3; Only used the 3 flight tracks (V019, V021, and V034) as used in Fig 8 of Di Biagio et al. (2019)
							470	0.9335		
							520	0.9474		
							590	0.9586		
							660	0.9637		
							880	0.9686		
							950	0.9686		
Formenti et al.[6]	AMMA	Aircraft	Menaka, Mali 16.5°N, 2.5°E	300 – 5300	11 June 2006 (JJA)	0.1 – 9	370	0.9268	0.0024	
							470	0.9477	0.0024	
							520	0.964	0.00235	
							590	0.9765	0.002425	
							660	0.9817	0.002425	
							880	0.9874	0.002525	
							950	0.9886	0.00245	

Johnson and Osborne[7]	Gerbils	Aircraft	Western Sahara 15.75°N, 6.88°W	2000 – 5000	18 to 29 June 2007 (JJA)	0.1 – 3	550	0.9705	0.00044	Directly measured – M1; PCASP-100 X and SID-2 (Wing); See their figure 6a; Optical diameter.
Müller et al.[8]	SAMUM-2	Ground-based	Cape Verde 14.9N, 23.5W	100	February 2008 (DJF)	0.1 – 10	450 550 950	0.91 0.96 0.98		Directly measured – M5.0; aerodynamic diameter; See their figure 4
Ryder et al.[9]	Fennec	Aircraft	Mali and Mauritania 24°N, 6°W	0 – 5500	17 to 26 June 2011 (JJA)	0.1 – 3	550	0.9670	0.0024	Directly measured – M1; See their figure 7a
Denjean et al.[10]	ADRIMED	Aircraft	Western Mediterranean 39.25°N, 9.05°E	3000 – 5000	16 June to 3 July 2013 (JJA)	0.01 – 5	530	0.95	0.0125	Directly measured – M4; Electric mobility and optical; Wing and in-cabin; See their figure 8; Diameter range of 0.01 – 12 µm for bulk scattering and 0.01 – 5

										µm for bulk extinction.
Ryder et al.[11]	AER-D	Aircraft	Between Cape Verde Islands and the Canary Islands 21.34°N, 19.03°W	1830	2 to 24 August 2015 (JJA)	0.1 – 3	550	0.9477	0.0157	Directly measured – M1; See their figure 12
				2150		0.1 – 3	550	0.9768	0.0071	
				2750		0.1 – 3	550	0.9679	0.0091	
				3057		0.1 – 3	550	0.9760	0.0073	
				3303		0.1 – 3	550	0.9707	0.0092	
				3508		0.1 – 3	550	0.9702	0.0092	
				3671		0.1 – 3	550	0.9811	0.0057	
				4125		0.1 – 3	550	0.9731	0.0082	
Denjean et al.[12]	DACCIWA	Aircraft	Gulf of Guinea 6.5N, 2.5E	3000 – 3800	29 June to 15 July 2016 (JJA)	0.01 – 5	550	0.92	0.02	Directly measured – M4.5; See their figure 7; We took those above 3km with low values of scattering angstrom exponent

*M1: PSAP (Radiance Research Inc.) measured bulk absorption at one wavelength (0.567 um), and nephelometer (model 3563, TSI Inc.) measured bulk scattering at three wavelengths (0.45, 0.55, and 0.70 um); by combing SSA was obtained at 0.55 um.

*M1.5: PSAP (Radiance Research Inc.) measured bulk absorption at three wavelengths (0.47, 0.532, and 0.66 um), and nephelometer (model 3563, TSI Inc.) measured bulk scattering at three wavelengths (0.45, 0.55, and 0.70 um); by combing SSA was obtained at 0.55 um.

*M2: PSAP (Radiance Research Inc.) measured bulk absorption at one wavelength (0.537 um), MAAP (Thermo Fisher Inc.) measured bulk absorption at one wavelength (0.637 um), and nephelometer (model 3563, TSI Inc.) measured bulk scattering at three wavelengths (0.45, 0.55, and 0.70 um); by combing SSA was obtained at 0.537 and 0.637 um.

*M3: Aethalometer (model AE31, Magee Sci.) measured bulk absorption at seven wavelengths (0.37, 0.47, 0.52, 0.59, 0.66, 0.88, and 0.95 um) and nephelometer (model 3596, TSI Inc.) measured bulk scattering at three wavelengths (0.45, 0.55, and 0.70 um); by combing them, SSA was obtained at the seven wavelengths (0.37, 0.47, 0.52, 0.59, 0.66, 0.88, and 0.95 um), in which SSA at 0.37, 0.88 and 0.95 um comes from extrapolation.

*M4: Light extinction monitor (model CAPS-PMex, Aerodyne Research) measured bulk extinction at one wavelength (0.53 um), and nephelometer (model 3563, TSI Inc.) measured bulk scattering at three wavelengths (0.45, 0.55, and 0.70 um); by combing them, SSA was obtained at 0.53 um.

*M4.5: Light extinction monitor (model CAPS-PMex, Aerodyne Research) measured bulk extinction at one wavelength (0.53 um), nephelometer (model 3563, TSI Inc.) measured bulk scattering at three wavelengths (0.45, 0.55, and 0.635 um), and PSAP measured bulk absorption at three wavelengths (0.467, 0.52, and 0.66 um); by combing them, SSA was obtained at 0.44, 0.55, and 0.66 um.

*M5.0: SOAP (Spectral Optical Absorption Photometer) is configured such that particles are collected on a fiber filter (Pallflex E70/2075W) after passing through an inlet, and which measurement of transmittance and reflectance is done by an optical spectrometer (Control Development Inc., CDI2DMPP-UV-VIS) before it is pumped out of the chamber. The transmittance and reflectance are used to calculate the spectral absorption and scattering coefficients.

Table S- 2: The dust complex refractive indices for selected and AeroCom models. The information for the selected models can be found in the highlighted references, while information on the AeroCom models is obtained directly from the website: https://wiki.met.no/aerocom/optical_properties (last assessed: 1 October 2020; see also Sand et al.[13]).

Models	Dust Refractive Index	Wavelength	Shape treatment/Method for optical properties	References	Comments
Selected Models					
WRFChem	1.53 - 0.003i	550	Spherical/Mie Theory	Zhao et al.[14]	Used OPAC for the refractive index of other aerosols and for dust longwave
IMPACT	1.53-0.0014i	550 nm	Spherical/Look-up table based on Mie Theory	Xu and Penner[15]; Ito and Kok[16]	
ARPEGE-Climat (CNRM)	1.51-0.008i	550nm	Spherical/Mie Theory	Nabat et al.[17]	See their Table 6
GISS	1.56 - 0.0014i	550nm	Spherical/Mie Theory	Miller et al.[18]	Based on SW refractive index from Petterson et al.[19] in Barbados. Longwave values are based on measurements by Volz[20].

CESM	1.53-0.002i	550nm	Spherical/Mie Theory	Kok et al.[21]	Based on OPAC database
GEOSChem	1.56-0.0014i	550nm	Spherical/Mie Theory	Kok et al.[22]	Based on the refractive index from Sinyuk et al.[23]
AeroCom Models					
CAM5-ATRAS	1.513-0.002074i	550 nm	Spherical/Mie Theory	Matsui[24] and Matsui and Mahowald[25]	Obtained from Sand et al.[13]
ECHAM6.3-HAM2.3	1.450-0.0010i	550 nm	Spherical/Mie Theory	Tegen et al. [26]	
ECHAM6.3-SALSA2.0	1.53-0.0011i	550 nm	Spherical/Mie Theory	Kokkola et al.[27]	
GEOS-i33p2	1.53 -0.0078 i	550 nm	Spherical/Mie Theory	Colarco et al.[28]	
GISS-ModelE2p1p1-OMA	1.564-0.0020i	550 nm	Spherical/Mie Theory	Koch et al.[29]	
INCA	1.52-0.00147i	550 nm	Spherical/Mie Theory	Balkanski et al.[30] and Schulz et al.[31]	

NorESM2	1.53-0.0024i	550 nm	Spherical/Mie Theory	Seland et al. [32]	
OsloCTM3v1.01	1.55-0.0031i	550 nm	Spherical/Mie Theory	Lund et al.[33]	

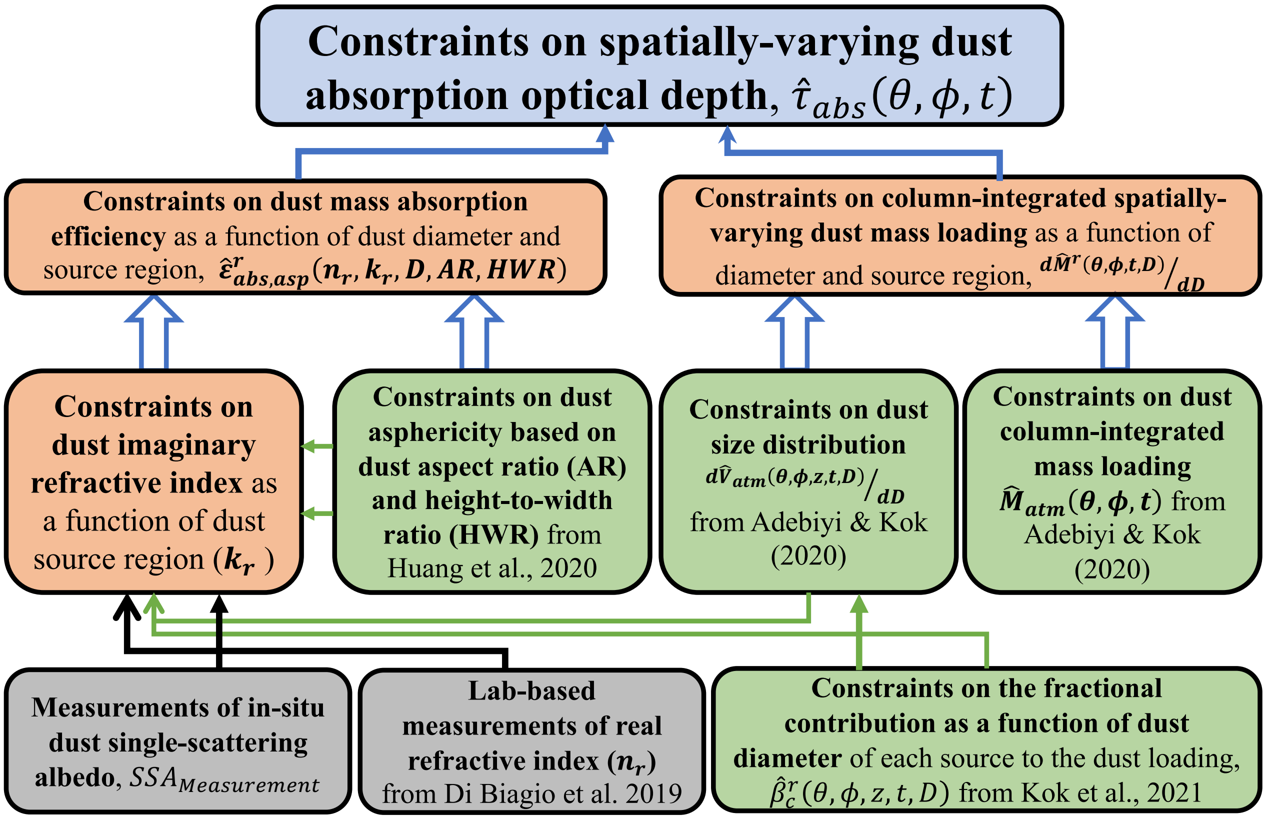

Figure S- 1: ***Schematics illustrating the methodology used to constrain dust absorption optical depth*** *(Blue box)**.** Boxes in orange are other observationally informed constraints or estimates obtained in this study, while boxes in green are observationally informed constraints previously published in other studies. Boxes in grey are measurements used as part of this study.*

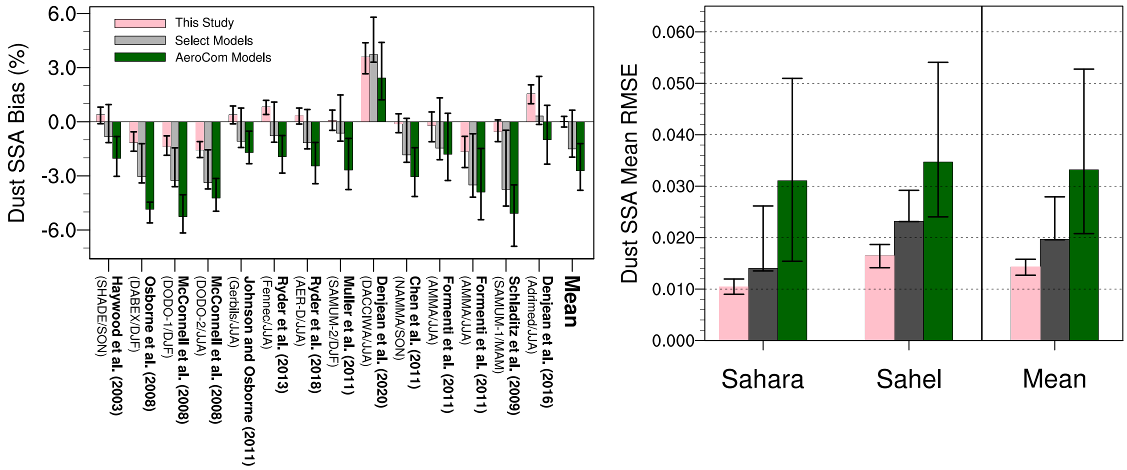

Figure S- 2: ***The bias in dust single-scattering albedo (SSA) estimates.*** *(a) The normalized dust SSA bias (%) for this study (pink bars), an ensemble of selected models (dark grey bars), and AeroCom models (dark green bars) compared for the same diameter and height range against the in-situ SSA measurements (see Table S-1). (b) The dust SSA root-mean-square error for the Sahara, the Sahel, and all of North Africa relative to the in-situ measurements.*

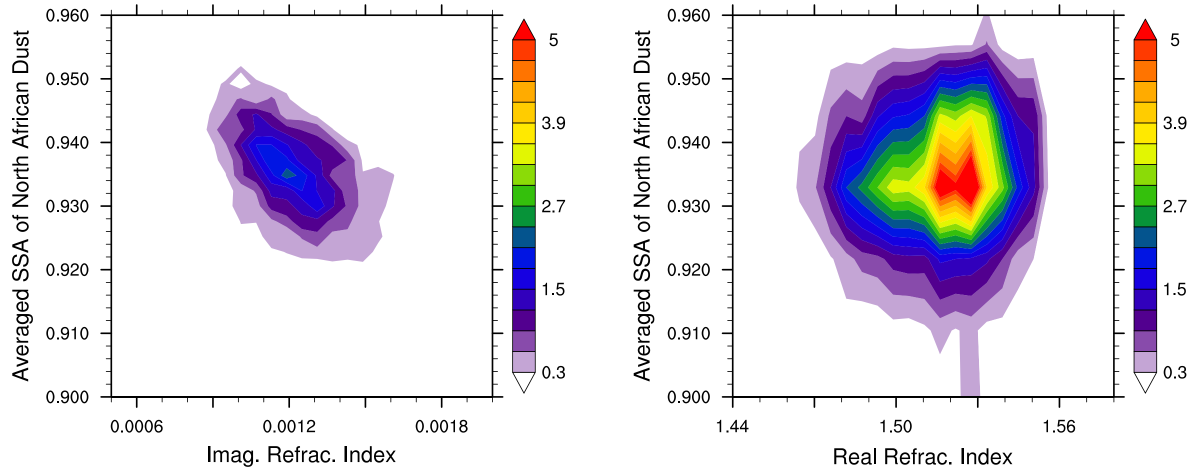

Figure S- 3: Joint probability distribution between (left) averaged single-scattering albedo and dust imaginary refractive index for North African dust at 550 nm wavelength, and (right) averaged single-scattering albedo and dust real refractive index for North African dust at 550 nm wavelength.

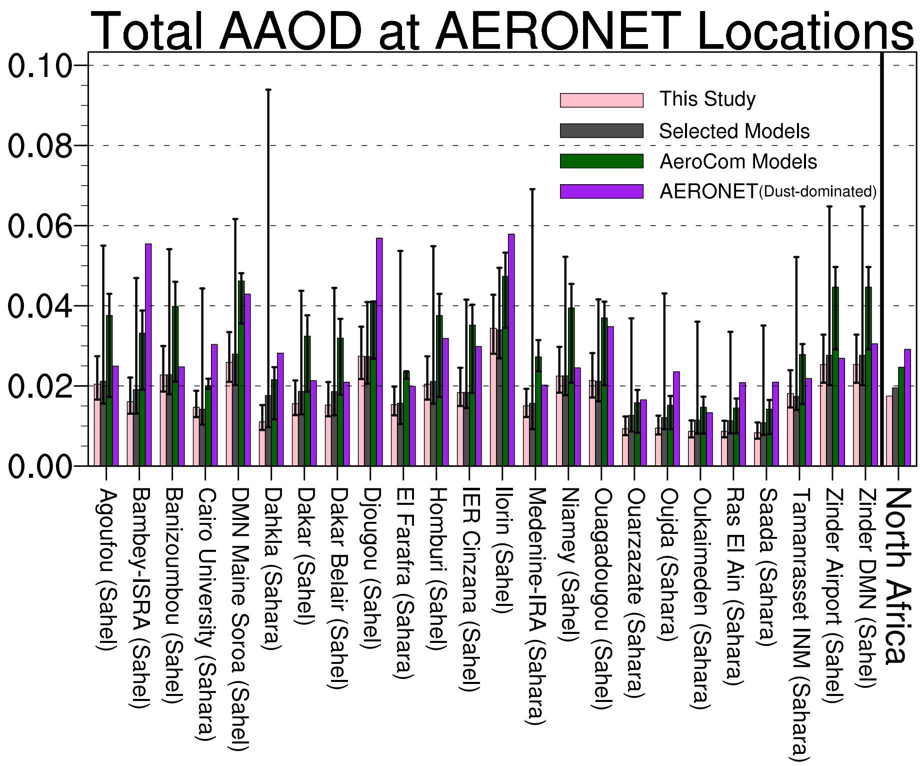

Figure S- 4: Same as Figure 3f, but for individual dust-dominated AERONET stations identified by red stars in Figure 3a-c.

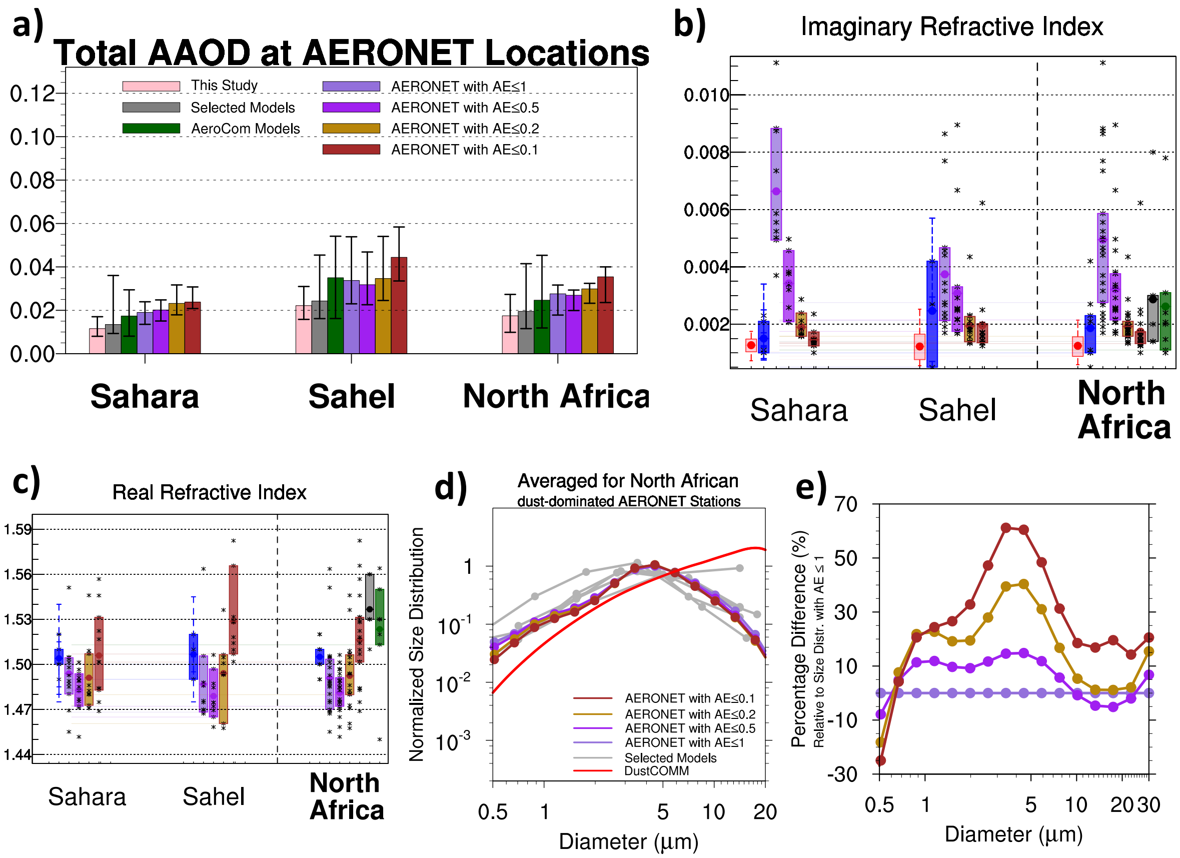

Figure S- 5: AERONET retrievals over dust-dominated North African locations exhibit consistent differences with observational constraints on AAOD, size distribution, and refractive index, regardless of the Angstrom exponent value used. The sensitivity analysis is conducted for Angstrom exponent (AE) values of 1, 0.5, 0.2, and 0.1. (a) Same as the total AAOD in Figure 3f, (b) Same as the imaginary refractive index in Figure 2c, (c) the real part of the refractive index in (b) above, (d) the same as the normalized size distribution in Figure 4c, and (e) the percentage difference between the AERONET-retrieved size distribution for other AE values and to the size distribution for AE=1.

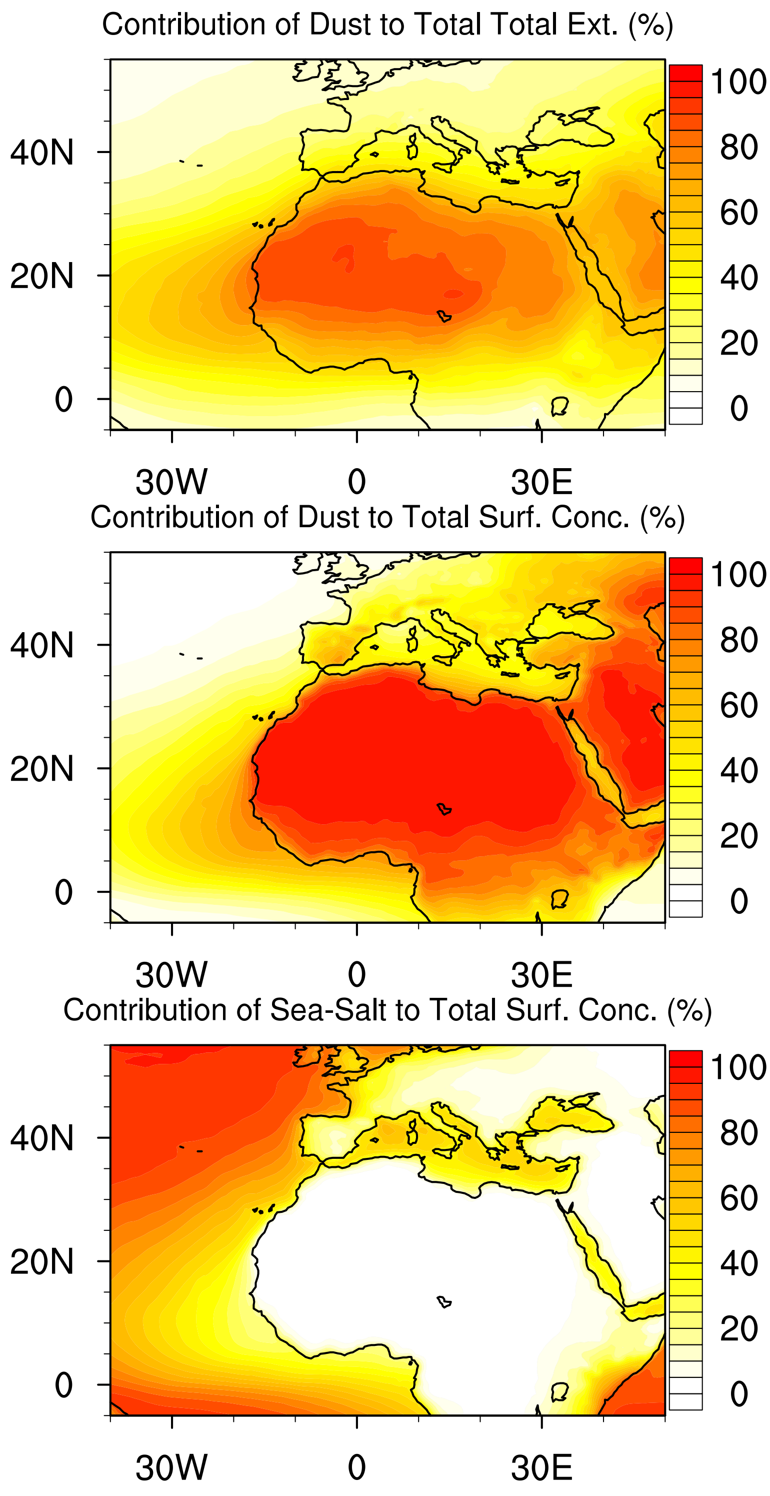

Figure S- 6: The upper and middle panels are the percentage contribution (%) of dust aerosols to the total aerosol extinction and total surface mass concentration, respectively. The lower panel shows the contribution of sea-salt aerosols to the total surface mass concentration. All datasets are obtained from MERRA-2 reanalysis.

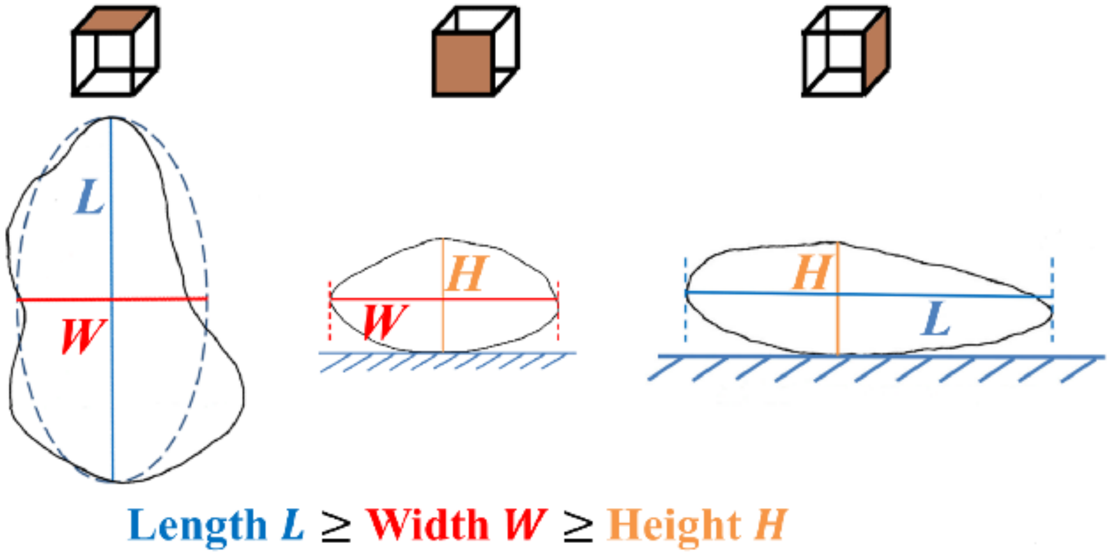

Figure S- 7: A schematic of the three dimensions of an aspherical dust particle. To estimate the dust optical properties, the shape is represented as an ellipsoid with a defined length, width, and height. See section S-4 for details.

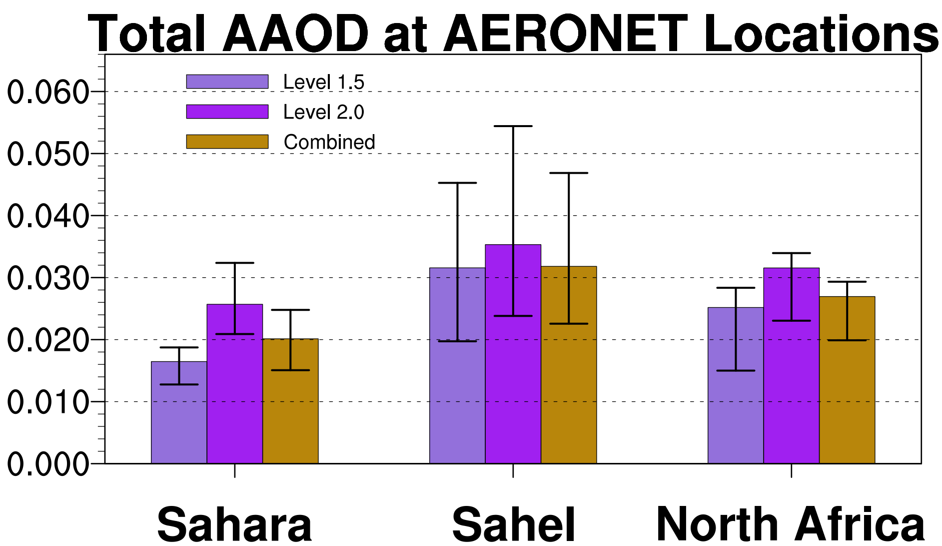

Figure S- 8: Similar to Fig. 3f but for AERONET Level-1.5, Level-2.0, and combined, as described in the Methods.

Supplementary Text

Section S-1: In-Situ Dust single-scattering Albedo Measurements

We compiled direct measurements of dust single-scattering albedo taken during major field campaigns over North Africa (see Table S-1). These campaigns span between 2000 and 2016 and include the SaHAran Dust Experiment (SHADE; [1]), Dust And Biomass burning Experiment (DABEX; [2]), Dust Outflow and Deposition to the Ocean project (DODO; [3]), Saharan Mineral Dust Experiments (SAMUM; [4,34]), African Monsoon Multidisciplinary Analysis project (AMMA), NASA AMMA (NAMMA; [6,35]), Geostationary Earth Radiation Budget Intercomparisons of Long-wave and Shortwave radiation experiment (GERBILS; [7]), Fennec 2011 [9], Aerosol Direct Radiative Impact on the regional climate in the MEDiterranean region (ADRIMED; [10]), AERosol Properties – Dust (AER-D; [11]), and Dynamics-Aerosol-Chemistry-Clouds Interactions in West Africa (DACCIWA; [12]).

While most of the reported measurements were taken on board aircraft, only the SAMUM measurement used ground-based instruments [4,34]. For most of these campaigns, the scattering coefficients were measured by the nephelometer, and the absorption coefficients were measured by the Particle Soot Absorption Photometer (PSAP; Table S-1). Other instruments used include the Aethalometer, which measures bulk absorption, and the light extinction monitor, which measures bulk extinction. Both the nephelometer and the PSAP are usually mounted inside the aircraft cabin behind the aircraft inlet. Furthermore, four major aircraft inlets were used in front of the nephelometer and the PSAP. These include (1) the Rosemount inlet with a 50% transmission efficiency at around 3 μm in optical diameter (Figure S1 of Ryder et al. [11]; (2) the AVIRAD inlet with a 50% transmission efficiency at 12 μm in optical diameter (Table 2 & Figure S2 in Denjean et al.[10]); (3) the Community aerosol inlet [10,12] with a 50% transmission efficiency at 5 μm in optical diameter (Table 2 & Figure S2 in Denjean et al.[10]); (4) the low turbulent inlet [36] with a 50% transmission efficiency at around 12 μm in aerodynamic diameter. Due to the particle loss and enhancement processes (including diffusive loss, gravimetric loss, inertial loss, electrophoretic loss, and thermophoretic loss)[9], coarse-sized dust aerosols can barely enter the nephelometer and the PSAP, and most aircraft studies using the nephelometer and the PSAP only measured dust single-scattering albedo (SSA) in the accumulation mode. Nevertheless, our measurement compilation also includes studies and other instruments with larger inlets that accommodate coarser-sized dust particles than measured by PSAP alone (up to approximately 9 μm; see Table S-1).

We used only reported SSA estimates with direct measurements of dust bulk scattering and absorption coefficients at one or multiple wavelengths. This contrasts with indirect SSA estimates, which, although these may use the measurements of dust size distribution, are calculated based on Mie theory, assuming a certain dust refractive index value and ignoring dust asphericity. However, the reported directly measured SSA estimates often do not rely on such assumptions of dust properties and therefore are less subject to biases and have a lower uncertainty range than indirect SSA estimates [11]. Specifically, these uncertainties are mostly associated with instrument calibrations or potential contamination by other aerosol species, such as biomass-burning aerosols or urban pollution [10,12,37,38]. In this study, we carefully selected studies that reported direct SSA measurements, ignoring those where the above-mentioned uncertainties are not addressed. For example, we did not use the SSA measurement from Ref.[39] due to potential uncertainties associated with the corrections to the nephelometer scattering and absorption and mixing with biomass aerosols [1]. For studies that included details of the measurement's environmental conditions or other information to help discriminate each data point, we selected only the data points that better represent the dust SSA. For example, in Ref.[12], we selected dust SSA measurements that are above 3 km and also have a lower value of scattering angstrom exponent as these measurements are more likely to be representative of the dusty Saharan air layer. Similarly, in Ref.[4], we selected only the measurements in a high-dust environment with a smaller potential for biomass-burning aerosol contamination.

To put these SSA measurements on a similar footing, we used the campaign mean SSA estimates, which correspond to a representative longitude and latitude location. To do so, we applied a weighting parameter, ϖ_j, for each measurement at the same wavelength from the j^{th} study. For studies that reported campaign mean SSA estimates or reported SSA estimate that is attributed to only one height level, $\varpi_j = 1$. For studies with multiple reported SSA measurements as a function of height, we took additional steps, estimating the weighting parameter based on the reported uncertainties and the climatological contribution of dust at that level to the total column dust loading. That is, for each reported height level j^z, we defined the weighting parameter as:

$$\varpi_{j^z} = \frac{f_{j^z} / \sigma_{s,j^z}}{\sum_{j^z=1}^{N_{j^z}} \left(f_{j^z} / \sigma_{s,j^z} \right)} \quad when\ N_{j^z} > 1 \qquad (S1.1)$$

Where ϖ_{j^z} is the weighting parameter that corresponds to each reported height level j^z, with reported uncertainty estimate, σ_{s,j^z}; N_{j^z} is the number of reported altitude levels for the j^{th} study; and f_{j^z} is the fractional contribution of the dust mass at height level j^z to the column dust mass loading. We obtained f_{j^z} from an ensemble of selected climate and chemical transport model simulations (see Table S-2 for details on the models). Furthermore, the above Eqn. S1.1 is such that $\sum_{j^z=1}^{N_{j^z}} \varpi_{j^z} = \varpi_j = 1$. Therefore, the campaign mean SSA estimate for the measurement from the j^{th} study is, therefore:

$$SSA_j^{insitu} = \sum_{j^z=1}^{N_{j^z}} SSA_{j^z} \cdot \varpi_{j^z} \qquad (S1.2)$$

Finally, for measurements that used aerodynamic diameter [4,5], we converted the diameter range to volume-equivalent diameter using Ref.[40]. However, conversion of the diameter range for measurements with optical diameter requires knowledge of dust minerology and other dust properties that is not available for all the studies, and as such it is beyond the scope of this study [40].

Section S-2: Estimates of dust single-scattering albedo corresponding to the in-situ measurements.

To obtain constraints on the dust imaginary refractive index (k_r) using Eqn. 1 in the main text, we estimated the dust SSA calculated for the same location and season and over the same height and diameter ranges as for the *in-situ* measurements (Table S-1). Specifically, we calculated the dust SSA as the extinction-weighted sum of the SSA of dust particles generated from each of the major dust source regions (Sahara and Sahel regions) reaching the measurement location. That is:

$$\mathrm{SSA}_{\text{This Study}}(\theta_j, \phi_j, t_j) = \sum_{r=1}^{N_r} \begin{bmatrix} \widehat{SSA}_{D_j,Z_j}^{j,r}(\theta_j, \phi_j, t_j, n_r, k_r, AR, HWR) \times \\ \hat{f}_{ext,D_j,Z_j}^{j,r}(\theta_j, \phi_j, t_j, n_r, k_r, AR, HWR) \end{bmatrix} \quad (S2.1)$$

The first parameter on the right, $\widehat{SSA}_{D_j,Z_j}^{j,r}$, is the estimate of dust SSA generated by source region r at the j^{th} measurement location with longitude θ_j, latitude ϕ_j, season t_j, and height range Z_j, as well as for dust size bin of median diameter D_j (between minimum D_j^{min} and maximum D_j^{max} diameters; see table S-1 for details). The second parameter on the right of Eqn. S2.1, $\hat{f}_{ext,D_j,Z_j}^{j,r}$, is the constraint on the fractional contribution of each source region to the overall dust extinction at the j^{th} measurement location. Both $\hat{f}_{ext,D_j,Z_j}^{j,r}$ and $\widehat{SSA}_{D_j,Z_j}^{j,r}$ depend on the layer-integrated dust size distribution $\left(\frac{d\hat{V}_{Z_j}^{j,r}}{dD_j}\right)$, the dust refractive indices (n_r, k_r), and dust shape parameters (AR – Aspect ratio and HWR – Height-to-Width ratio). We describe in the following paragraphs the details of the framework used to estimate these parameters. Since this framework is developed for any given location, including the measurement locations, we drop hereafter the subscript/superscript j.

For the first parameter in Eqn. S2.1, we compute the $\widehat{SSA}_{D,Z}^{r}$ associated with each source region (r) as:

$$\widehat{SSA}_{D,Z}^{r}(\theta, \phi, t, n_r, k_r, AR, HWR) = \frac{\int_{D^{min}}^{D^{max}} \frac{\hat{Q}_{sca,asp}^{r}(n_r, k_r, D, AR, HWR)}{D} \frac{d\hat{V}_Z^r(\theta, \phi, t, D)}{dD} dD}{\int_{D^{min}}^{D^{max}} \frac{\hat{Q}_{ext,asp}^{r}(n_r, k_r, D, AR, HWR)}{D} \frac{d\hat{V}_Z^r(\theta, \phi, t, D)}{dD} dD} \quad (S2.2)$$

Where $\widehat{SSA}_{D,Z}^{r}$ is integrated over a defined height range Z and diameter range D^{min} to D^{max} with median diameter D that depend on the instrument inlet (Table S-1). In addition, $\widehat{SSA}_{D,Z}^{r}$ depends on the layer-integrated dust size distribution, $\frac{d\hat{V}_Z^r}{dD}$, and the size-resolved single-particle dust optical properties – the dust scattering efficiency, $\hat{Q}^r_{sca,asp}$, and extinction efficiency, $\hat{Q}^r_{ext,asp}$, for each dust source region, r.

To obtain constraints on the source-resolved layer-integrated dust size distribution, $\frac{d\hat{V}^r_Z}{dD}$ in Eqn. S2.2, we used the datasets from DustCOMM, where we multiplied the constraint on the dust size distribution [41] with the constraint on the fractional contribution by each dust source region to the overall dust concentration [42]. That is:

$$\frac{d\hat{V}^r_Z}{dD} = \sum_{k=1}^{N_Z} \tilde{\alpha}_Z(\theta, \phi, t, z_k) \cdot \hat{\beta}^r_c(\theta, \phi, t, z_k, D) \cdot \frac{d\hat{V}_{atm}(\theta, \phi, t, z_k, D)}{dD} \qquad (S2.3)$$

Where $\tilde{\alpha}_Z$ is the fraction of dust mass loading as a function of height obtained from an ensemble of selected model simulations for a given location and season (see Table S-2 for the model simulations used); For each location and season, we normalized $\tilde{\alpha}_Z$ over the a defined height range Z such that $\sum_{k=1}^{N_Z} \tilde{\alpha}_Z(\theta, \phi, t, z_k) = 1$; where k is the individual altitude level (z_k) within the height range Z, with the total number of N_Z. The second parameter in Eqn. S2.3, $\hat{\beta}^r_c$, is the DustCOMM constraint on the fractional contribution of each source region (r) to the total dust concentration as a function of dust diameter for a given location, height, and season. This constraint on $\hat{\beta}^r_c$, with details described in [42], combines observational constraints on dust properties and dust aerosol optical depth with an ensemble of climate model simulations to determine the relative contribution of different major source regions to the global dust cycle. For each location, height, season, and diameter, we normalized $\hat{\beta}^r_c$ such that: $\sum_{r=1}^{N_r} \hat{\beta}^r_c(\theta, \phi, t, z_k, D) = 1$. The third parameter in Eqn. S2.3, $\frac{d\hat{V}_{atm}}{dD}$, is the constraint on dust volume size distribution obtained from the DustCOMM dataset (see Ref.[41,43]. Similar to $\hat{\beta}^r_c$, the dust volume size distribution is normalized, such that $\int_{D^{min}}^{D^{max}} \frac{d\hat{V}_{atm}(\theta, \phi, t, z_k, D)}{dD} = 1$.

In addition to the source-resolved layer-integrated dust size distribution in Eqn. S2.2, we obtained constraints on the source-resolved single-particle dust scattering, $\hat{Q}^r_{sca,asp}$, dust absorption, $\hat{Q}^r_{abs,asp}$ and dust extinction efficiencies, $\hat{Q}^r_{ext,asp}$ ($= \hat{Q}^r_{sca,asp} + \hat{Q}^r_{abs,asp}$). These dust optical properties not only depend on source-resolved complex refractive indices (n_r and k_r), but also on dust diameter and dust shape, defined by the dust aspect ratio (AR) and height-to-width ratio (HWR). For a given wavelength, the dust diameter directly influences the dust optical properties through its influence on the size parameter ($x = \frac{\pi D}{\lambda}$). In addition, an irregularly-shaped dust particle has a larger surface area than a volume-equivalent sphere, which can lead to higher extinction and absorption than a spherical dust particle of the same volume [22,44]. Therefore, we accounted for dust asphericity by approximating dust as tri-axial ellipsoidal particles described by AR and HWR. Since the Lorenz-Mie theory used in most climate models is invalid for aspherical dust particles, we obtained the single-particle dust optical properties from the single-scattering database of Ref.[45]. This database precomputes the single-particle dust optical properties for a range of AR, HWR, size parameter, and dust refractive index (see section

S-4). We thus obtained ensemble-averaged dust optical properties by integrating over the probability distributions of the globally-representative values of AR and HWR obtained by Ref.[44]. Unlike $\frac{d\hat{V}_Z^r}{dD}$, the size-resolved single-particle dust optical properties are assumed to be invariant over the reported height range, Z, but vary regionally based on the source-resolved refractive index values (n_r and k_r).

Like $\widehat{SSA}_{D,Z}^r$ in Eqn. S2.2, we can also estimate the fractional contribution to the overall dust extinction as a function of dust source region (r). That is:

$$\hat{f}_{ext,D,Z}^r(\theta,\phi,t,n_r,k_r,AR,HWR) = \frac{\int_{D^{min}}^{D^{max}}\left[\frac{\hat{Q}_{ext,asp}^r(n_r,k_r,D,AR,HWR)}{D}\,\frac{d\hat{V}_Z^r(\theta,\phi,t,D)}{dD}\right]dD}{\sum_{r=1}^{N_r}\int_{D^{min}}^{D^{max}}\left[\frac{\hat{Q}_{ext,asp}^r(n_r,k_r,D,AR,HWR)}{D}\,\frac{d\hat{V}_Z^r(\theta,\phi,t,D)}{dD}\right]dD} \qquad (S2.4)$$

Where $\hat{f}_{ext,D,Z}^r$ is integrated over the diameter range D and height range Z. In addition, the dust size distribution, $\frac{d\hat{V}_Z^r}{dD}$, and the single-particle dust optical properties ($\hat{Q}_{ext,asp}^r$) are as described above in Eqn. S2.2 & S2.3.

Section S-3: Using *in-situ* SSA measurements at other wavelengths to constrain the refractive index of North African dust at 550 nm wavelength.

The procedure in Methods constrained the dust imaginary refractive index (k_r) at 550 nm. Although most of the *in-situ* SSA measurements have values at 550 nm (see Table S-1), the *in-situ* SSA measurements used do not have to be at the same wavelength. For studies with no reported measurement at 550 nm but with more than one reported measurement at other wavelengths (below or above 550 nm), we interpolated to obtain the equivalent SSA value at 550 nm (see section S-1). Similarly, for studies where only one SSA measurement is reported but at wavelengths other than 550nm, we took additional steps to include such measurements in the procedure, constraining the dust imaginary refractive index at 550 nm. In this case, we only allowed measurements between 500 nm and 600 nm. Specifically, we obtained equivalent constraints on dust imaginary refractive index at 550 nm using the spectral distribution of Ref.[46] dust refractive index for each source region r. To do so, we estimated $\mathrm{SSA}^{j}_{\mathrm{This\ Study}}$ in Eqn. 1, and consequently $\widehat{SSA}_{D,Z}^r$ and $\hat{f}_{ext,D,Z}^r$ (Eqn. S2.2 and Eqn. S2.4), using the dust refractive index at the wavelength λ. This yielded a constraint on k_r^λ, the dust imaginary refractive index at wavelength λ, that is proportional to our constraints on dust imaginary refractive index at 550 nm (k_r). That is: $k_r^\lambda = \psi k_r$, where $\psi = k_{r,DB}^\lambda / k_{r,DB}$ – the ratio between Di Biagio et al.'s dust imaginary refractive index at wavelength λ and at 550 nm. Implicitly, we have assumed that the regional variability in refractive index values at the wavelength λ is proportional to the variability at 550 nm. In addition, we computed only for the imaginary part of the refractive index since the real part is mostly spectrally invariant in the visible spectrum [46].

Section S-4: Constraints on single-particle dust optical properties

We obtained constraints on single-particle dust optical properties for an irregularly shaped dust particle by approximating it as a tri-axial ellipsoidal particle described by the dust aspect ratio (AR) and height-to-width ratio (HWR). Specifically, we used a look-up table containing size-resolved and refractive index-resolved dust optical properties (including the dust extinction efficiency ($\hat{Q}^{r}_{ext,asp}$), dust scattering efficiency ($\hat{Q}^{r}_{sca,asp}$), dust absorption efficiency ($\hat{Q}^{r}_{abs,asp}$), and single-scattering albedo) of aspherical dust approximated as ellipsoids. This look-up table was computed based on the single-scattering database of ellipsoidal dust by Ref.[45] and it contains the following variables: (1) 200 dust geometric diameters logarithmically ranging from 0.2 µm to 20 µm, and corresponding to the dust diameter range used in DustCOMM; (2) 10 real refractive indices (n = 1.32, 1.36, 1.39, 1.43, 1.47, 1.51, 1.54, 1.62, 1.69, and 1.76) and 13 imaginary refractive indices (k = 0.0005, 0.0008, 0.0012, 0.0018, 0.0027, 0.0041, 0.0062, 0.0094, 0.0143, 0.0217, 0.1000, 0.1733, and 0.3000).

Consequently, we obtained the size- and refractive index-resolved dust optical properties by integrating this single-scattering database[45] with the globally-averaged dust shape distributions obtained by Ref.[44]. The single-scattering database of [45] combines four computational methods (Lorenz-Mie theory, T-matrix method, discrete dipole approximation, and an improved geometric optics method) to compute the single-scattering properties of ellipsoidal dust for a wide range of aspect ratio (AR $= \frac{L}{W}$; Fig. 10), height-to-width ratio (HWR $= \frac{H}{W}$), size parameter, and refractive index. Ref.[44] compiled dozens of measurements of AR and HWR worldwide, and they found that both HWR and the deviation of AR from unity (AR-1) follow lognormal distributions. In the study, we took the medians of AR and HWR as 1.70 ± 0.03 and 0.40 ± 0.07, respectively, and the geometric standard deviations of AR-1 and HWR, respectively as 0.70 ± 0.02 and 0.73 ± 0.09, after the globally-averaged distributions of AR and HWR[44]. By combining Ref.[45] database and Ref.[44]'s shape distributions, we obtained the size- and refractive index-resolved look-up table on the optical properties of tri-axial ellipsoidal dust. Further details can be found in Ref.[40].

For an arbitrary combination of real and imaginary refractive indices, we estimated an approximated value of dust optical properties (i.e., $\hat{Q}^{r}_{ext,asp}$, $\hat{Q}^{r}_{sca,asp}$, $\hat{Q}^{r}_{abs,asp}$) using the lookup table. Specifically, we computed a matrix of $N_n \; X \; N_k$ grid which covered the range of expected values of these optical properties and obtained the values corresponding to our defined n and k using a logarithm interpolation. In addition, although the standard look-up table is provided at 550 nm wavelength, we can estimate the dust optical properties of any wavelengths in the shortwave spectrum using look-up tables at 470, 370, 590, 550, 520, 660, 780, 880, and 950 nm. This is useful to compute the dust SSA corresponding to measurements at wavelengths other than 550 nm (see section S-1 and Methods).

Section S-5: Quantification of uncertainties in our constraints on dust properties.

We quantified the uncertainties in our constraints on the source-resolved dust imaginary refractive index (k_r; Eqn. 1) and size-resolved dust AAOD ($\hat{\tau}_{abs}$; Eqn. 2) by using a non-parametric procedure based on the bootstrap method [47,48]. Specifically, we quantified the uncertainties by randomly selecting a value from the probability distributions representing each of the input variables in the calculations of k_r and $\hat{\tau}_{abs}$. This process was then repeated a large number of times to obtain the corresponding probability distribution for $\hat{\tau}_{abs}$ and k_r. Therefore, this bootstrap method allowed us to propagate the uncertainties in each of the input variables that would otherwise be difficult to obtain if we considered the parametric quantification of errors in each of them. One important consideration with this approach is that the relevant input variables are assumed to be independent of each other. We describe below the detailed steps used to obtain these uncertainties.

Dust imaginary refractive index:

1. Within the range of uncertainties defined for each measurement (see Table 1), we randomly select single-scattering albedo values assuming a Gaussian distribution for the j^{th} location and season.

2. In addition, from the observationally-informed DustCOMM dataset [41–43,49], we randomly selected a realization from the probability distributions of the dust size distribution $\left(\frac{d\hat{V}_{atm}(\theta_j,\phi_j,t_j,z_j,D_j)}{dD_j}\right)$ and the fractional contribution of each dust source to the overall dust concentration, $\hat{\beta}_c^r(\theta_j, \phi_j, t_j, z_j, D_j)$, over the j^{th} measurement's location and season.

3. With Eqn. S2.3, we used these variables from step (2) above to account for the fractional contribution of each dust region, r, to the dust size distribution $\left(\frac{d\hat{V}_{Z_j}^r}{dD_j}\right)$ reaching the j^{th} measurement's location (θ_j, ϕ_j) during season t_j. We integrated this size distribution over the defined height range over which the measurements were made (see Table S-1). The fraction of dust mass, $\tilde{\alpha}_Z(\theta_j, \phi_j, t_j, z_j)$ as a function of height is taken from the selected models (see Table S-2), where one of the six models is drawn randomly for each iteration.

4. To estimate dust $\mathrm{SSA}^{j}_{\mathrm{This\ Study}}(\theta_j, \phi_j, t_j)$ for each measurement location, we randomly selected a value of the dust real refractive index from a Gaussian distribution with mean 1.51 and standard deviation 0.03 (after Di Biagio et al.,

2019) and did this separately for the Sahara and Sahel source regions. The imaginary refractive index (k_r) is the parameter to be determined (see next step).

5. We iterated over a range of dust imaginary refractive index values to determine the value that optimally reproduces the compilation of in-situ dust SSA measurements obtained in step (1) above. We defined an initial range of dust imaginary refractive index of $k^r_{range} = 0.00051 - 0.01$, based on literature measurements [1,20,46,50–52]. For each iteration, we obtained the single-particle dust scattering efficiency ($\hat{Q}^r_{sca,asp}$) and extinction efficiency ($\hat{Q}^r_{ext,asp}$) using the look-up table described in Section S-4. Subsequently, we determined the dust $\mathrm{SSA}^j_{\mathrm{This\ Study}}$ (Eqn. S2.1) by calculating $\widehat{SSA}^r_{D,Z}$ (Eqn. S2.2), $\hat{f}^r_{ext,D,Z}$ (Eqn. S2.4), and by integrating them over the diameter range between D^{min}_j and D^{max}_j corresponding to that sampled by each measurements (see Table S-1).

6. We repeated step 1-5 a large number of times to obtain the probability distribution for k_r.

Dust aerosol absorption optical depth:

Similar to our procedure for quantifying the probability distribution of the dust imaginary refractive index, we randomly selected realizations of the DustCOMM column-integrated dust mass loading, $\widehat{M}_{atm}(\theta, \phi, t)$, dust size distribution $\left(\frac{d\widehat{V}_{atm}(\theta,\phi,t,D)}{dD}\right)$ and the fractional contribution by each dust source to the overall dust concentration, $\hat{\beta}^r_c(\theta, \phi, t, D)$, over each location [41–43,49].

We used these randomly selected values to obtain constraints on the contribution of each source region r to the column-integrated dust mass size distribution $\left(\frac{d\widehat{M}^r}{dD};\ g\ m^{-3}\right)$ reaching the location θ, ϕ, during the season t. Here, $\frac{d\widehat{M}^r(\theta,\phi,t,D)}{dD} = \widehat{M}_{atm}(\theta, \phi, t) \cdot \frac{d\widehat{V}^r_Z(\theta,\phi,t,D)}{dD}$, and $\frac{d\widehat{V}^r_Z(\theta,\phi,t,D)}{dD}$ is obtained from Eqn. S2.3.

In addition, we randomly selected values for the dust refractive index (n_r, k_r) and dust density (ρ_d) to obtain constraints on the size-resolved mass absorption efficiency for dust particles generated by each source region r in Eqn. 2. That is, $\hat{\varepsilon}^r_{abs,asp} = \frac{3}{2\rho_d} \cdot \frac{\hat{Q}^r_{abs,asp}(n_r,k_r,AR,HWR,D)}{D}$. The randomly selected value of n_r is drawn from a Gaussian distribution with a mean of 1.51 and standard deviation of 0.03 (after DiBiagio et al., 2019) and is drawn separately for the Sahara and Sahel dust source regions. Similarly, k_r is randomly drawn from the probability distribution obtained above. Lastly, ρ_d is drawn from a Gaussian distribution with a mean of $2500\ kg\ m^{-3}$ and a standard deviation of $200\ kg\ m^{-3}$ [22,53,54], and is drawn separately for the Sahara and Sahel dust source regions.

Subsequently, we obtained $\hat{\varepsilon}^{r}_{abs,asp}$, which we then combined with $\frac{d\hat{M}^{r}}{dD}$ from step (2) above to obtain $\frac{d\hat{\tau}_{abs}}{dD}$.

We repeated steps 1-3 a large number of times to obtain the probability distribution of $\frac{d\hat{\tau}_{abs}}{dD}$.

Section S-6: Calculating dust absorption properties for the selected and AeroCom models.

Dust aerosol absorption optical depth for the selected models: To calculate the equivalent model dust AAOD for the selected models, we used an equation similar to Eqn. 2 (see Methods).

$$\frac{d\tilde{\tau}^{m_S}_{abs}(\theta,\phi,t)}{\mathrm{dD}} = \sum_{r=1}^{N_r} \tilde{\varepsilon}_{abs,sph}(n^{m_S},k^{m_S},D) \cdot \frac{d\widetilde{M}^{r}_{m_S}(\theta,\phi,t,D)}{dD} \qquad \text{(S7.1)}$$

and $\tilde{\varepsilon}_{abs,sph}(n^{m_S},k^{m_S},D) = \frac{3}{2\rho_d} \cdot \frac{\tilde{Q}_{abs,sph}(n^{m_S},k^{m_S},D)}{D}$

Where $\tilde{\tau}^{m_S}_{abs}$ is the simulated dust AAOD for each selected model m_s. Since the selected-model size-resolved dust loadings are available for discrete particle size bins, we fitted a power law distribution on the column-integrated size-resolved dust mass load values between adjacent model bins.

In addition, to better compare our constraints on dust AAOD ($\hat{\tau}_{abs}$) to the estimated dust AAOD from selected models ($\tilde{\tau}^{m_S}_{abs}$), we also estimate the absorption properties that is generated by dust sources over North Africa. Specifically, we used the constraint on the fractional contribution of each source region (r) to the total dust loading $\hat{\beta}^{r}_{c}$ [42,49] obtain the dust mass distribution, $\frac{d\widetilde{M}^{r}_{m_S}(\theta,\phi,t,D)}{dD}$ for each of the selected models. Furthermore, we used the dust complex refractive index (n^{m_S}, k^{m_S}) for each selected model, m_S, reported in the literature (see Table S-2) to estimate the dust absorption efficiency, $\tilde{Q}_{abs,sph}$. Since models generally use spatially invariant refractive indices and assume that dust particles are spherical, we used Lorenz-Mie theory to estimate each model's $\tilde{Q}_{abs,sph}$, which is thus the same for the Sahara and the Sahel regions.

Furthermore, we used similar procedure as the one above to estimate the contribution of each of the input parameters to the overall bias in the simulated dust AAOD (Fig. 3). Specifically, we replaced each of the input dust properties in the estimation of the simulated size-resolved dust AAOD for each of the six selected models in Eqn. S7.1. These parameters replaced include: (1) the dust size distribution, where we replaced $\frac{d\widetilde{V}^{r}_{m_S}(\theta,\phi,t,D)}{dD}$ by $\frac{d\widehat{V}^{r}_{Z}\,(\theta,\phi,t,D)}{dD}$; (2) the column-integrated dust mass load, where we replaced $\widetilde{M}^{r}_{m_S}(\theta,\phi,t,D)$ by $\widehat{M}_{atm}\,(\theta,\phi,t,D)$; (3) the dust refractive index, where we replaced n^{m_S}

and k^{m_s} by n_r and k_r to calculate the single-particle dust optical properties. Note that in this case, we used Lorenz-Mie theory, which assumes a spherical shape; (4) the dust shape, where the spherical representation of dust shape is replaced by an aspherical representation obtained by the measurement compilation of [44] of the dust aspect ratio (AR) and height-to-width ratio (HWR) used in the calculation of single-particle dust optical properties. Specifically, we replaced $\tilde{Q}_{abs,sph}(n^{m_s}, k^{m_s}, D)$ by $\tilde{Q}_{abs,sph}(n^{m_s}, k^{m_s}, \text{AR}, \text{HWR}, D)$, and as such, we used the single-scattering database of Meng et al. [45] that incorporates the effects of dust asphericity on the dust optical properties instead of the Lorenz-Mie theory used in most global models. Given the non-linear, non-additive nature of this procedure, the combined effect of this bias does not directly reproduce the overall bias, indicating that the residual is non-zero.

Dust single-scattering albedo for selected and AeroCom models: To calculate the equivalent dust SSA for the selected models m_s we used an equation similar to Eqn. S2.2 above. That is:

$$\widetilde{SSA}^{j,m_s}_{D_j,Z_j}(\theta_j, \phi_j, t_j, n^{m_s}, k^{m_s}) = \frac{\int_{D^{min}}^{D^{max}} \frac{\tilde{Q}_{sca,sph}(n^{m_s}, k^{m_s}, D)}{D} \frac{d\tilde{V}^{j,m_s}_{Z_j}(\theta_j, \phi_j, t_j, D)}{dD_j}\, dD}{\int_{D^{min}}^{D^{max}} \frac{\tilde{Q}_{ext,sph}(n^{m_s}, k^{m_s}, D)}{D} \frac{d\tilde{V}^{j,m_s}_{Z_j}(\theta_j, \phi_j, t_j, D)}{dD_j}\, dD} \quad (S6.2)$$

Where $\widetilde{SSA}^{j,m_s}_{D_j,Z_j}$ is the estimated dust single-scattering albedo of the selected model, m_S, corresponding to the j^{th} measurement with diameter range D_j, height range Z_j, season t_j, and representative location (θ_j, ϕ_j). The simulated dust size distribution is $\frac{d\tilde{V}^{j,m_s}_{Z_j}}{dD_j}$; and the $\tilde{Q}_{sca,sph}$ and $\tilde{Q}_{ext,sph}$ are respectively the scattering and extinction efficiency, similar to $\tilde{Q}_{abs,sph}$ above, that uses the model complex refractive index and Lorenz-Mie theory.

Unlike for the selected models, the dust size distribution information was not available for the AeroCom models at the time of this analysis. Hence, to calculate the equivalent dust SSA for AeroCom models over a certain height range and diameter range, we used the estimated column-integrated dust SSA for the selected models to scale the column-integrated dust SSA for the AeroCom models. That is:

$$\widetilde{SSA}^{j,m_A}_{D_j,Z_j}(\theta_j, \phi_j, t_j, n^{m_A}, k^{m_A}) = \widetilde{\mathrm{SSA}}^{j,m_A}(\theta_j, \phi_j, t_j, n^{m_A}, k^{m_A}) \cdot \tilde{\alpha}^j_{D_j,Z_j}(\theta_j, \phi_j, t_j) \quad (S6.3a)$$

and

$$\tilde{\alpha}^j_{D_j,Z_j}(\theta_j, \phi_j, t_j) = \frac{\widetilde{SSA}^{j,m_s}_{D_j,Z_j}(\theta_j, \phi_j, t_j, n^{m_s}, k^{m_s})}{\widetilde{\mathrm{SSA}}^{j,m_s}(\theta_j, \phi_j, t_j, n^{m_s}, k^{m_s})} \quad (S6.3b)$$

Where $\widetilde{SSA}^{j,m_s}_{D_j,Z_j}$ is defined in Eqn. S6.2 for the selected models, m_S, that corresponds to the diameter range D_j, and height range Z_j of the j^{th} measurement, and $\widetilde{SSA}^{j,m_s}$ is the same as $\widetilde{SSA}^{j,m_s}_{D_j,Z_j}$ but estimated over the entire diameter range up to 20µm and over the entire atmospheric column. In addition, $\widetilde{SSA}_{D_j,Z_j}^{j,m_A}$ is the simulated dust SSA for each of the AeroCom models, m_A, at the same representative location of the j^{th} SSA measurement, over the diameter range D_j, and height range Z_j, and $\widetilde{\mathrm{SSA}}^{j,m_A}$ is the column-integrated SSA value estimated from each AeroCom models as the ratio of the AeroCom's dust scattering optical depth (dust AOD – dust AAOD) to the AeroCom's dust extinction optical depth (dust AOD).

Finally, we assumed that both the selected models and the AeroCom models simulations represent the present-day climatology, although the selected model simulations are generally between 2004-2008 [43], and the AeroCom model simulations are for the year 2010.

<u>**Supplementary References:**</u>

1. Haywood, J. *et al.* Radiative properties and direct effect of Saharan dust measured by the C-130 aircraft during Saharan Dust Experiment (SHADE): 2. Terrestrial spectrum. *Journal of Geophysical Research* **108**, 8578 (2003).
2. Osborne, S. R. *et al.* Physical and optical properties of mineral dust aerosol during the Dust and Biomass-burning Experiment. *Journal of Geophysical Research* **113**, 00C03 (2008).
3. McConnell, C. L. *et al.* Seasonal variations of the physical and optical characteristics of Saharan dust: Results from the Dust Outflow and Deposition to the Ocean (DODO) experiment. *Journal of Geophysical Research* **113**, 14S05 (2008).
4. Schladitz, A. *et al.* In situ measurements of optical properties at Tinfou (Morocco) during the Saharan Mineral Dust Experiment SAMUM 2006. *Tellus, Series B: Chemical and Physical Meteorology* **61**, 64–78 (2009).
5. Chen, G. *et al.* Observations of Saharan dust microphysical and optical properties from the Eastern Atlantic during NAMMA airborne field campaign. *Atmospheric Chemistry and Physics* **11**, 723–740 (2011).
6. Formenti, P. *et al.* Airborne observations of mineral dust over western Africa in the summer Monsoon season: spatial and vertical variability of physico-chemical and optical properties. *Atmospheric Chemistry and Physics* **11**, 6387–6410 (2011).
7. Johnson, B. T. & Osborne, S. R. Physical and optical properties of mineral dust aerosol measured by aircraft during the GERBILS campaign. *Quarterly Journal of the Royal Meteorological Society* **137**, 1117–1130 (2011).
8. Müller, T., Schladitz, A., Kandler, K. & Wiedensohler, A. Spectral particle absorption coefficients, single scattering albedos and imaginary parts of refractive indices from ground based in situ measurements at Cape Verde Island during SAMUM-2. *Tellus, Series B: Chemical and Physical Meteorology* **63**, 573–588 (2011).
9. Ryder, C. L. *et al.* Optical properties of Saharan dust aerosol and contribution from the coarse mode as measured during the Fennec 2011 aircraft campaign. *Atmospheric Chemistry and Physics* **13**, 303–325 (2013).
10. Denjean, C. *et al.* Size distribution and optical properties of African mineral dust after intercontinental transport. *Journal of Geophysical Research: Atmospheres* **121**, 7117–7138 (2016).
11. Ryder, C. L. *et al.* Coarse-mode mineral dust size distributions, composition and optical properties from AER-D aircraft measurements over the tropical eastern Atlantic. *Atmospheric Chemistry and Physics* **18**, 17225–17257 (2018).
12. Denjean, C. *et al.* Overview of aerosol optical properties over southern West Africa from DACCIWA aircraft measurements. *Atmospheric Chemistry and Physics* **20**, 4735–4756 (2020).
13. Sand, M. *et al.* Aerosol absorption in global models from AeroCom phase III. *Atmospheric Chemistry and Physics* **21**, 15929–15947 (2021).
14. Zhao, C. *et al.* Uncertainty in modeling dust mass balance and radiative forcing from size parameterization. **13**, 10733–10753 (2013).
15. Xu, L. & Penner, J. E. Global simulations of nitrate and ammonium aerosols and their radiative effects. *Atmospheric Chemistry and Physics* **12**, 9479–9504 (2012).

16. Ito, A. & Kok, J. F. Do dust emissions from sparsely vegetated regions dominate atmospheric iron supply to the Southern Ocean? *Journal of Geophysical Research: Atmospheres* **122**, 3987–4002 (2017).
17. Nabat, P. *et al.* A 4-D climatology (1979–2009) of the monthly tropospheric aerosol optical depth distribution over the Mediterranean region from a comparative evaluation and blending of remote sensing and model products. *Atmospheric Measurement Techniques* **6**, 1287–1314 (2013).
18. Miller, R. L., Tegen, I. & Perlwitz, J. Surface radiative forcing by soil dust aerosols and the hydrologic cycle. *Journal of Geophysical Research D: Atmospheres* **109**, (2004).
19. Patterson, E. M., Gillette, D. A. & Stockton, B. H. Complex index of refraction between 300 and 700 nm for Saharan aerosols. *Journal of Geophysical Research* **82**, 3153–3160 (1977).
20. Volz, F. E. Infrared Optical Constants of Ammonium Sulfate, Sahara Dust, Volcanic Pumice, and Flyash. *Applied Optics* **12**, 564 (1973).
21. Kok, J. F., Albani, S., Mahowald, N. M. & Ward, D. S. An improved dust emission model - Part 2: Evaluation in the Community Earth System Model, with implications for the use of dust source functions. *Atmospheric Chemistry and Physics* **14**, 13043–13061 (2014).
22. Kok, J. F. *et al.* Smaller desert dust cooling effect estimated from analysis of dust size and abundance. *Nature Geoscience* **10**, 274–278 (2017).
23. Sinyuk, A., Torres, O. & Dubovik, O. Combined use of satellite and surface observations to infer the imaginary part of refractive index of Saharan dust. *Geophysical Research Letters* **30**, (2003).
24. Matsui, H. Development of a global aerosol model using a two-dimensional sectional method: 1. Model design. *Journal of Advances in Modeling Earth Systems* **9**, 1921–1947 (2017).
25. Matsui, H. & Mahowald, N. Development of a global aerosol model using a two-dimensional sectional method: 2. Evaluation and sensitivity simulations. *Journal of Advances in Modeling Earth Systems* (2017) doi:10.1002/2017MS000937.
26. Tegen, I. *et al.* The global aerosol-climate model echam6.3-ham2.3 -Part 1: Aerosol evaluation. *Geoscientific Model Development* **12**, 1643–1677 (2019).
27. Kokkola, H. *et al.* SALSA2.0: The sectional aerosol module of the aerosol-chemistry-climate model ECHAM6.3.0-HAM2.3-MOZ1.0. *Geoscientific Model Development* (2018) doi:10.5194/gmd-11-3833-2018.
28. Colarco, P., Silva, A., Chin, M. & Diehl, T. Online simulations of global aerosol distributions in the NASA GEOS - 4 model and comparisons to satellite and ground - based aerosol optical depth. **115**, (2010).
29. Koch, D., Jacob, D., Tegen, I., Rind, D. & Chin, M. Tropospheric sulfur simulation and sulfate direct radiative forcing in the Goddard Institute for Space Studies general circulation model. *Journal of Geophysical Research: Atmospheres* **104**, 23799–23822 (1999).
30. Balkanski, Y., Schulz, M., Claquin, T., Moulin, C. & Ginoux, P. Global Emissions of Mineral Aerosol: Formulation and Validation using Satellite Imagery. in (2004). doi:10.1007/978-1-4020-2167-1_6.

31. Schulz, M., Cozic, A. & Szopa, S. LMDzT-INCA dust forecast model developments and associated validation efforts. *IOP Conference Series: Earth and Environmental Science* (2009) doi:10.1088/1755-1307/7/1/012014.
32. Seland, Ø. *et al.* Overview of the Norwegian Earth System Model (NorESM2) and key climate response of CMIP6 DECK, historical, and scenario simulations. *Geoscientific Model Development* **13**, 6165–6200 (2020).
33. Lund, M. T. *et al.* Concentrations and radiative forcing of anthropogenic aerosols from 1750 to 2014 simulated with the Oslo CTM3 and CEDS emission inventory. *Geoscientific Model Development* (2018) doi:10.5194/gmd-11-4909-2018.
34. Müller, T., Schladitz, A., Kandler, K. & Wiedensohler, A. Spectral particle absorption coefficients, single scattering albedos and imaginary parts of refractive indices from ground based in situ measurements at Cape Verde Island during SAMUM-2. *Tellus, Series B: Chemical and Physical Meteorology* **63**, 573–588 (2011).
35. Chen, G. *et al.* Observations of Saharan dust microphysical and optical properties from the Eastern Atlantic during NAMMA airborne field campaign. *Atmospheric Chemistry and Physics* **11**, 723–740 (2011).
36. Clarke, A. D. *et al.* Size distributions and mixtures of dust and black carbon aerosol in Asian outflow: Physiochemistry and optical properties. *Journal of Geophysical Research* **109**, 15S09 (2004).
37. Kandler, K. *et al.* Electron microscopy of particles collected at Praia, Cape Verde, during the Saharan Mineral Dust Experiment: particle chemistry, shape, mixing state and complex refractive index. *Tellus B: Chemical and Physical Meteorology* **63**, 475–496 (2011).
38. Weinzierl, B. *et al.* Airborne measurements of dust layer properties, particle size distribution and mixing state of Saharan dust during SAMUM 2006. *Tellus B: Chemical and Physical Meteorology* **61**, 96–117 (2009).
39. Haywood, J. M., Francis, P. N., Glew, M. D. & Taylor, J. P. Optical properties and direct radiative effect of Saharan dust: A case study of two Saharan dust outbreaks using aircraft data. *Journal of Geophysical Research: Atmospheres* **106**, 18417–18430 (2001).
40. Huang, Y., Adebiyi, A. A., Formenti, P. & Kok, J. F. Linking the Different Diameter Types of Aspherical Desert Dust Indicates That Models Underestimate Coarse Dust Emission. *Geophysical Research Letters* **48**, (2021).
41. Adebiyi, A. A. & Kok, J. F. Climate models miss most of the coarse dust in the atmosphere. *Science Advances* **6**, eaaz9507 (2020).
42. Kok, J. F. *et al.* Contribution of the world's main dust source regions to the global cycle of desert dust. *Atmospheric Chemistry and Physics* **21**, 8169–8193 (2021).
43. Adebiyi, A. A. *et al.* Dust Constraints from joint Observational-Modelling-experiMental analysis (DustCOMM): comparison with measurements and model simulations. *Atmospheric Chemistry and Physics* **20**, 829–863 (2020).
44. Huang, Y. *et al.* Climate Models and Remote Sensing Retrievals Neglect Substantial Desert Dust Asphericity. *Geophysical Research Letters* **47**, (2020).
45. Meng, Z. *et al.* Single-scattering properties of tri-axial ellipsoidal mineral dust aerosols: A database for application to radiative transfer calculations. *Journal of Aerosol Science* **41**, 501–512 (2010).

46. Di Biagio, C. *et al.* Complex refractive indices and single-scattering albedo of global dust aerosols in the shortwave spectrum and relationship to size and iron content. *Atmospheric Chemistry and Physics* **19**, 15503–15531 (2019).
47. Efron, B. & Gong, G. A Leisurely Look at the Bootstrap, the Jackknife, and Cross-Validation. *The American Statistician* **37**, 36–48 (1983).
48. Chernick, M. R. *Bootstrap Methods*. *Climate Change 2013 - The Physical Science Basis* vol. 53 (John Wiley & Sons, Inc., 2007).
49. Kok, J. F. *et al.* Improved representation of the global dust cycle using observational constraints on dust properties and abundance. *Atmospheric Chemistry and Physics* **21**, 8127–8167 (2021).
50. Kandler, K. *et al.* Chemical composition and complex refractive index of Saharan Mineral Dust at Izaña, Tenerife (Spain) derived by electron microscopy. *Atmospheric Environment* **41**, 8058–8074 (2007).
51. Sokolik, I., Andronova, A. & Johnson, T. C. Complex refractive index of atmospheric dust aerosols. *Atmospheric Environment. Part A. General Topics* **27**, 2495–2502 (1993).
52. Redmond, H. E., Dial, K. D. & Thompson, J. E. Light scattering and absorption by wind blown dust: Theory, measurement, and recent data. *Aeolian Research* **2**, 5–26 (2010).
53. Kaaden, N. *et al.* State of mixing, shape factor, number size distribution, and hygroscopic growth of the Saharan anthropogenic and mineral dust aerosol at Tinfou, Morocco. *Tellus B: Chemical and Physical Meteorology* **61**, 51–63 (2009).
54. Fratini, G., Ciccioli, P., Febo, A., Forgione, A. & Valentini, R. Size-segregated fluxes of mineral dust from a desert area of northern China by eddy covariance. *Atmospheric Chemistry and Physics* **7**, 2839–2854 (2007).